Visualization by x-ray tomography of void growth and coalescence leading to fracture in model materials

Arnaud Weck, David Wilkinson, E. Maire, H. Toda

May 13, 2008

A. Weck
McMaster University, Department of Materials Science and Engineering. 1280 Main Street West, Hamilton, ON, Canada. weckag@mcmaster.ca
D. Wilkinson
McMaster University, Department of Materials Science and Engineering. 1280 Main Street West, Hamilton, ON, Canada.
E. Maire
MATEIS INSA-Lyon, F-69621, France UMR CNRS 5510
H. Toda
Department of Production Systems Engineering, Toyohashi University of Technology, Toyohashi 441-8580, Japan.

Abstract

The literature contains many models for the process of void nucleation, growth and coalescence leading to ductile fracture. However, these models lack in depth experimental validation, in part because void coalescence is difficult to capture experimentally. In this paper, an embedded array of holes is obtained by diffusion bonding a sheet filled with laser-drilled holes between two intact sheets. The experiments have been performed with both pure copper and Glidcop. Using x-ray computed tomography, we show that void growth and coalescence (or linkage) is well captured in both materials. The Brown and Embury model for void coalescence underestimates coalescence strains due to constraining effects. However, both the Rice and Tracey model for void growth and the Thomason model for void coalescence give good predictions for copper samples when stress triaxiality is considered. The Thomason model however fails to predict coalescence for the Glidcop samples; this is primarily due to secondary void nucleation.

1 Introduction

Extensive experimental and modelling efforts have been done to better understand the ductile fracture process which involves void nucleation [1, 2, 3], growth [4, 5, 6, 7, 8, 9] and coalescence [6, 10, 11, 12, 13, 14, 15, 16]. However, lack of quantitative experimental data on the last stage of the fracture process limited the development of accurate models for failure prediction. Experimental data is difficult to obtain, because of the stochastic nature of void coalescence, the considerable number of voids, and difficulties with void observation inside the sample. Model materials were used to simplify ductile fracture analysis [17, 18, 19, 20, 21], but none successfully overcame the above challenges. In this paper, in order to visualize void growth and coalescence in a controlled manner model materials containing laser-drilled holes were fabricated. These materials consisted of a laser-drilled sheet diffusion-bonded between two intact (i.e. non-drilled) sheets; fabrication is described elsewhere [22]. The laser-drilled sheet has a thickness equal to the hole diameter resulting in a sample containing quasi-spherical holes. The holes are monitored using x-ray computed tomography. Because of the need for high quality diffusion bonding between the sheets, the samples fabricated to date are all copper based

(both high purity copper and Glidcop). The effect of material type, and the influence of secondary void population on coalescence has been investigated. Finally, results are analyzed and compared to the Rice and Tracey model for void growth, and the Brown and Embury and the Thomason models for void coalescence.

2 Experimental methods

The samples are made of high purity copper (99.999%) and Glidcop. The latter consists of a copper matrix containing 0.25% by wt. of aluminum in the form of a fine dispersion (∼50 nm in diameter) of aluminum oxide. The copper samples were tested at the Japanese synchrotron SPRing-8 on beamline BL20XU. Because this beamline uses monochromated x-rays at 30 keV and the voxel size used was 0.48 μm, the samples have a width of 0.25 mm, a thickness of 0.215 mm and a gage length of 2 mm. The hole diameter is 10 μm. Each sample contained a single sheet 10 μm thick containing an array of holes, embedded between two thicker sheets that were free of holes. The two copper samples tested contain a rectangular array of 176 holes oriented at 45° to the tensile axis and an array of 120 holes oriented at 75° to the tensile axis. In both cases, the center to center holes spacing in the array is chosen to be 20 μm and the local void volume fraction is therefore 6.5%. The Glidcop samples were tested at the European synchrotron ESRF on beamline ID15. This beamline uses white light at 60 keV and offered a voxel size of 1.6 μm. Therefore the samples have a width of 0.8 mm, a thickness of 1 mm and holes have a diameter of 40 μm. The two Glidcop samples tested contain a rectangular array of 168 holes oriented at 45° to the tensile axis and an array of 130 holes oriented at 90° to the tensile axis. In both cases, the center to center holes spacing in the array is chosen to be 80 μm and the local void volume fraction is therefore 6.5%. Glidcop samples have a tapered gage length of radius 10 mm to ensure that failure occurs in the middle of the sample. These samples also contained a single (40 μm thick) sheet with holes. The experimental set-up used at SPRing-8 and at ESRF are described in Uesugi et al. [23] and Di Michiel et al. [24] respectively. Tensile tests were performed at constant strain rate and at room temperature on a specially designed in situ tensile testing machine [25]. The specificity of the machine is an almost x-ray transparent PMMA tube which was used to transmit the load between the upper and lower grips of the machine. This permitted a 180° machine rotation without the frame hiding the beam. The machine was used in tension with a load cell of 1500 N and both load and displacement were recorded during the test. During the in-situ tomography experiments, the samples are deformed in tension and the test is stopped at various displacements in order to acquire a tomogram. Depending on how quickly the sample failed and on the number of interesting events occurring during the test, the number of tomograms acquired varied between samples (typically from 4 to 7). In order to acquire high resolution tomograms, the samples were held at a fixed displacement. The acquisition was started only after the sample had time to relax resulting in a constant load. The imaging time was about 10 minutes at SPRing-8 and closer to 30 seconds at ESRF.

3 Experimental results

In the following, tomograms are presented for the copper and Glidcop samples. The true stress-strain curves are then calculated and the fracture surfaces observed in a scanning electron microscope (SEM).

3.1 X-ray tomograms

Two samples were tested. They contained holes in a square array aligned at 75° and 45° with respect to the tensile axis, respectively. The macroscale tomograms are shown in Figures 1 and 2 where some transparency has been numerically applied to the matrix so that the voids which are in the middle of the sample can be seen. From these pictures one can see that void growth and coalescence are well captured. Furthermore, because the sample has small dimensions, the external shape of the whole sample can be visualized. The first point to notice is the inhomogeneous necking in the case of the copper sample (in-

volving shear band formation) compared to the more homogeneous necking for the Glidcop samples (Figures 1 and 2). The irregular necking is better seen on the minimum cross sections of the copper sample shown in Figure 5. The inhomogeneities are due to the large grain size in the copper sample (about 300 μm). In the Glidcop samples, the necking is more regular because of the small grain size (about 10 μm) and the presence of a fine dispersion of nanometric alumina particles that refines the scale of the plasticity. A close up from the tomography data showing hole growth and linkage is presented in Figure 3(a-d) and 4(a-d). It should be noticed that the copper holes shown in Figure 3(a) are somewhat less regular in shape than those made in the Glidcop samples (Figure 4(a)). These differences can be explained by the smaller hole size for the copper samples (10 μm) compared to the Glidcop samples (40 μm) which makes the diffusion bonding process during sample fabrication more difficult to control. Moreover, the small size accentuates shape anomalies. A comparison between copper and Glidcop samples at coalescence shows that failure occurs after less void elongation in the Glidcop samples. The normalized length of the void (defined as L/L_0 where L is the current length and L_0 the initial length) at coalescence for the high purity copper sample containing an array at 45° is 4.77 whereas that for the Glidcop sample is 2.54 for the same initial ratios of intervoid spacing over void diameter and the same void orientation. Finally, the strong necking in the 3D case unloads the parts of the sample away from the neck which prevents the holes from shearing at 45° and forces the sample to fail horizontally. Because coalescence occurs at lower strains in the Glidcop samples, the holes in the 45° case (Figure 4) cannot interact horizontally like in the copper sample and an instability oriented at 45° occurs between the voids. However, the sample cannot completely fail at 45° because, as in the copper samples, the neck controls the failure path leading to a zig-zag type of failure.

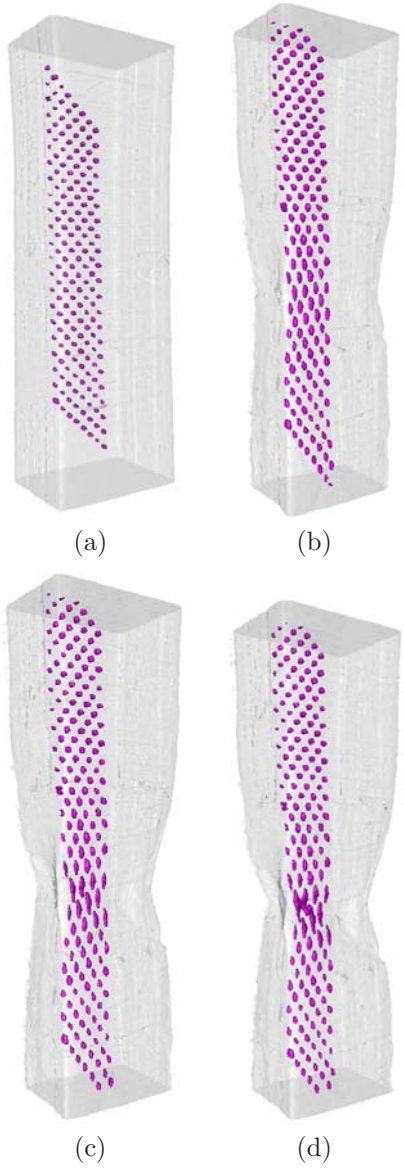

Figure 1: Tomographic reconstruction of a copper sample containing an array of laser drilled holes at 45° with respect to the tensile axis (vertical). The sample has been tested in-situ and the tomograms correspond to the following true strains (a) 0.00, (b) 0.50, (c) 0.77, (d) 1.01. Some transparency has been numerically applied to the material so that the holes can be visualized. The tensile direction is vertical.

3.2 In-situ tensile test results

The smallest cross sectional area can be extracted from Figures 1 and 2 in order to determine the true

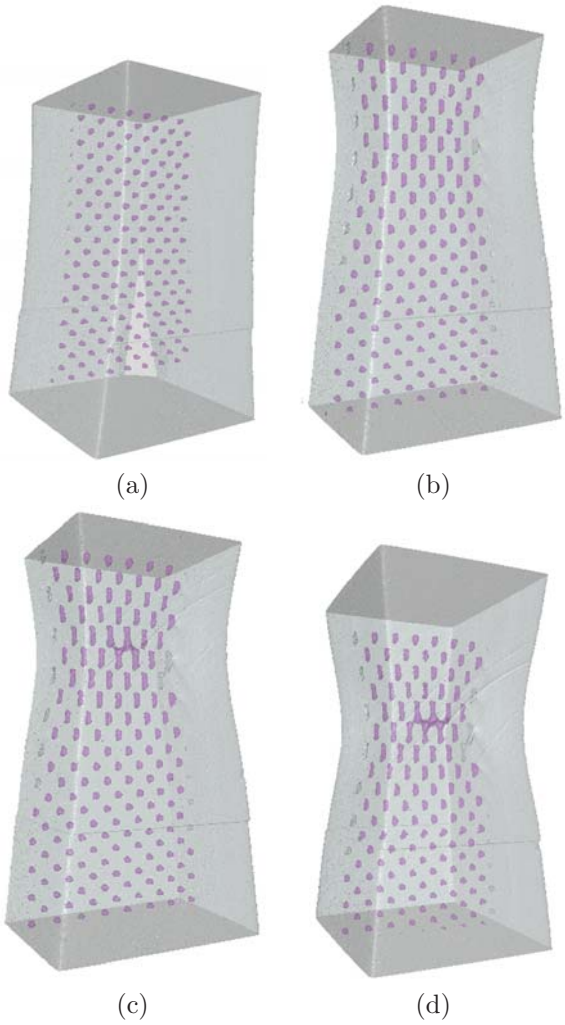

Figure 2: Tomographic reconstruction of a Glidcop sample containing an array of laser drilled holes at 45° with respect to the tensile axis (vertical). The sample has been tested in-situ and the tomograms correspond to the following true strains (a) 0.00, (b) 0.35, (c) 0.45, (d) 0.50. Some transparency has been numerically applied to the material so that the holes can be visualized. The tensile direction is vertical.

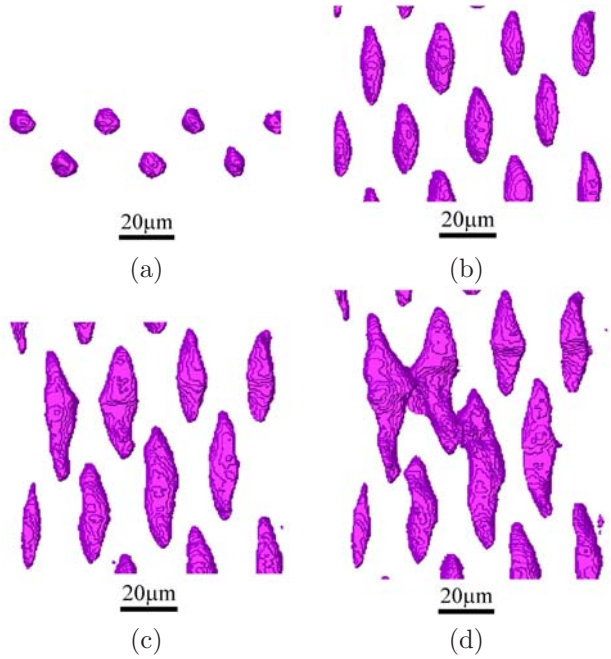

Figure 3: Close up from Figure 1 showing the hole growth and coalesence. The pictures have been taken at true strains of (a) 0.00, (b) 0.50, (c) 0.77, (d) 1.01.

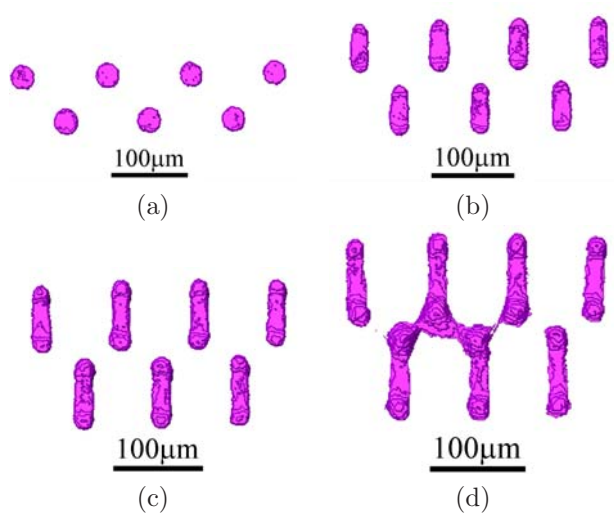

Figure 4: Close up from Figure 2 showing the hole growth and coalescence. The pictures have been taken at true strains of (a) 0.00, (b) 0.35, (c) 0.45, (d) 0.50.

stress and strain during necking. Figure 5 shows the evolution of the smallest cross sectional area as deformation proceeds for a copper sample with an array of holes at 45°. Using the image analysis software Amira^{TM}, the real cross sectional area without the voids A can be extracted. The true stress-strain curves prior to necking are calculated using equations 1 and 2 below where $s = L/A_0$ is the engineering stress and $e = (l - l_0)/l_0$ is the engineering strain (L is the load, A_0 the initial cross sectional area, l_0 and l the initial and current gage length respectively). After necking, equations 3 and 4 have to be used. The resulting true stress-strain curves for the two samples tested at SPRing-8 are shown in Figure 6. Because the volume fraction of voids is low, the flow curves are the same up to failure for each of the two void configurations studied.

$$\sigma = s(e + 1) \tag{1}$$

$$\varepsilon = ln(e + 1) \tag{2}$$

$$\sigma = \frac{L}{A} \tag{3}$$

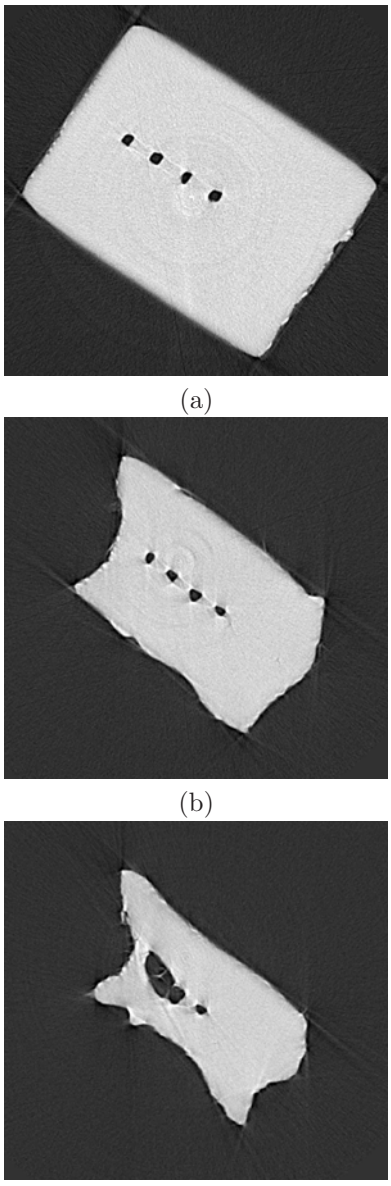

Figure 5: Smallest cross sectional areas extracted from the tomography reconstruction of a high purity copper sample containing an array of holes at 45° with respect to the tensile axis. The corresponding areas and true strains are respectively (a) 0.051 mm^2 and 0.00 (b) 0.023 mm^2 and 0.77 (c) 0.015 mm^2 and 1.20.

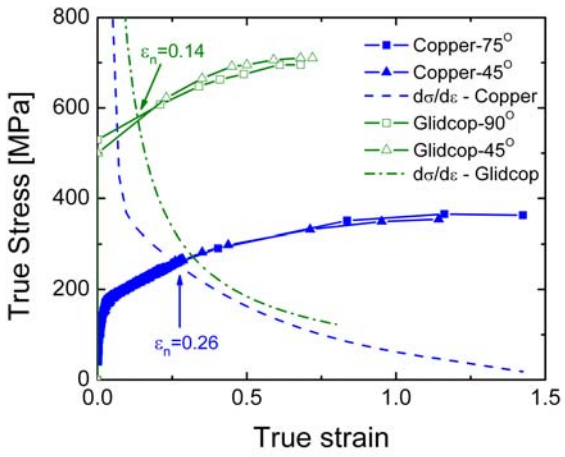

Figure 6: True stress-strain curves of two high purity copper and two Glidcop samples tested in tomography containing an array of holes oriented at various degrees with respect to the tensile axis.

$$\varepsilon = ln\left(\frac{A_0}{A}\right) \tag{4}$$

Because the Glidcop tensile samples have an initial shallow notch to force the specimen to break in the middle of the sample only equations 3 and 4 apply because there is no constant measure of the gage length that would be required in using equations 1 and 2. The current smallest cross sectional area is obtained as a function of strain from the reconstructed tomograms in the same way as for the copper samples. The true stress-strain curves are plotted in Figure 6. One can see that because of the smaller grain size and the alumina particles, Glidcop is much stronger than high purity copper (by about 400 MPa) and the failure strains are about half that of copper.

3.3 Fractography

The fracture surface of the copper and Glidcop samples tested in tomography were observed in an SEM and are shown in Figure 7. One can see that the ligament between the holes necks down to a line without any secondary void nucleation in the case of copper. This is attributed to the high purity of the sample

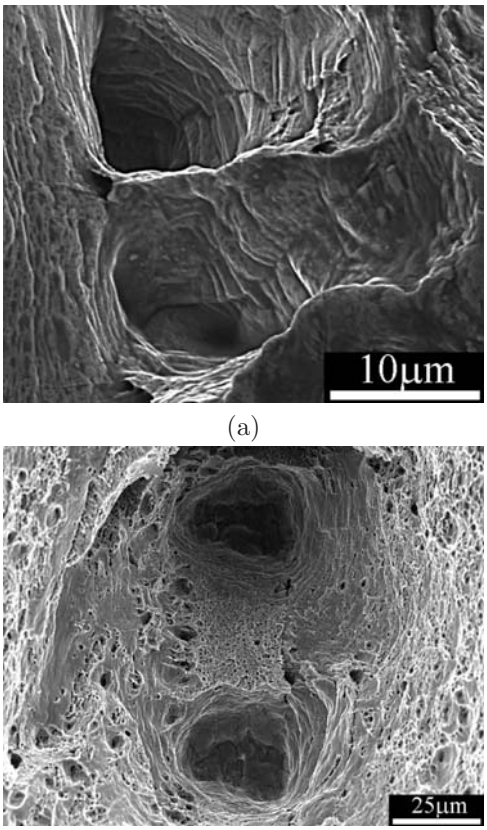

(a)

(b)

Figure 7: SEM images of fracture surfaces showing a close up on the ligament between two laser drilled holes in (a) copper and (b) Glidcop samples.

that prevents the nucleation of voids at impurities. Another interesting feature is the wavy markings on the hole surfaces which is attributed to a coarse slip mechanism in the sample. For the Glidcop samples however, coalescence does not occur by the necking of the ligament between the holes down to a line. Instead, coalescence is precipitated by the nucleation of a secondary population of voids between the main laser drilled holes. These secondary voids are nucleated at the fine alumina particles present in the Glidcop.

4 Comparison with existing models

The Rice and Tracey model [8] for void growth and the Brown and Embury model [14] and the Thomason model [26] for void coalescence can be compared to the experimental results. Comparison might also be done here using other models from the literature such as the Gurson [9] and the Rousselier models [27]. However, these models require several adjustable parameters which are not easily measured experimentally, thus making a quantitative comparison impossible. Furthermore, recent extensions of the Gurson model that have been proposed to account for void coalescence [28, 32] are based on the Thomason model [26]. Therefore, comparison to such models will not give more insight into the coalescence event.

4.1 Void growth: Rice and Tracey model

The integrated form of the Rice and Tracey equations for an initially spherical void of radius R_0 is that of Thomason [26]. They give the principal radii of the ellipsoidal void in the case of uniaxial tension in both tensile R_1 and transverse R_2 directions as follows:

$$R_1 = \left[\exp(D\varepsilon_1) + \frac{1+E}{D}\left(\exp(D\varepsilon_1) - 1\right)\right] R_0, \quad (5a)$$

$$R_2 = \left[\exp(D\varepsilon_1) - \frac{1+E}{2D}\left(\exp(D\varepsilon_1) - 1\right)\right] R_0, \quad (5b)$$

where

$$D = 0.558 \sinh\left(\frac{3}{2}\frac{\sigma_m}{Y}\right) + 0.008 \cosh\left(\frac{3}{2}\frac{\sigma_m}{Y}\right),$$

ε_1 is the total logarithmic strain integrated over the total strain path, σ_m is the mean stress and Y the yield stress. The parameters D and E are used in the Rice and Tracey model to vary the contribution of the volume and shape changing part to void growth respectively. In the case of pure copper, because the difference between the yield stress and the ultimate tensile stress (UTS) is high (more than a factor of 2), the material is assumed to be strongly hardening and the parameter $(1 + E)$ from equation 5 is equal to 5/3 as proposed by Rice and Tracey [8]. In the case of Glidcop, because its yield stress is high (Figure 6) and because the difference between yield stress and UTS is low (about a factor of 1.3), the material is assumed to be non-hardening with high mean stress and the parameter $(1 + E) = 2$. When using a constant stress triaxiality T of 0.33, one can see in Figure 8 that the Rice and Tracey model does not give good predictions of void growth. We have seen in the experimental section that the samples show a significant amount of necking prior to coalescence and therefore the changes in stress triaxiality cannot be neglected. In order to calculate the stress triaxiality σ_m/Y, the following equation by Bridgman [29] is used:

$$\frac{\sigma_m}{Y} = \frac{1}{3} + ln\left(\frac{a+2R}{2R}\right), \quad (6)$$

where a is the smallest cross sectional radius and R the neck radius. This equation has been initially defined for axisymmetric samples but has been shown by Zhang et al. [30] to be applicable to samples with rectangular cross section. It should be noted that the use of the Bridgman analysis and that of Zhang is only an approximation as they assume isotropic and uniform samples which is not strictly true for the copper samples. The parameters a and R can be extracted from Figures 1 and 2. Because the neck geometry can be different on each side of the sample, an averaged value of R is used. Also, because of the rather significant uncertainty in the measurements of the radius R and because of the asymmetry of the neck geometry (especially for the copper samples), the calculated values of stress triaxiality are somewhat prone to error. This is why the triaxiality results are compared in Figure 10 to the predicted values of the stress triaxiality as a function of strain given by equation 7:

$$\frac{\sigma_m}{Y} = \frac{1}{3} + ln\left(1 + \frac{1}{2}\sqrt{\varepsilon_1 - \varepsilon_n}\right) \quad (7)$$

where ε_1 is the true strain and ε_n the true strain at necking. Equation 7 is based on a relatively simple empirical expression given by Bridgman [29] for the neck ratio $a/R = \sqrt{|ln(A_0/A) - \varepsilon_n|}$ which is valid up to reductions in area of 95%. The true strain at

necking ε_n is found from the intersection of the true stress and the work hardening rate curves as a function of true strain and is shown in Figure 6. It takes the values of 0.26 and 0.14 for respectively copper and Glidcop. Equation 7 is in good agreement with the experimental results in Figure 10 and provides more consistent results. It is now possible to recalculate the values obtained from the Rice and Tracey equation by including the stress triaxiality variations as a function of strain from equation 7. The results from the model, shown in Figure 8, are now in much better agreement with the experimental results. Experimentally measured transverse void growth and that predicted by equation 5b for a constant triaxiality of 0.33 and for the varying triaxialities of copper and Glidcop samples are presented in Figure 9. As for void growth in the tensile direction, the Rice and Tracey predictions for transverse void growth are in good agreement with the experimental results (up to the linkage event) when the changes in stress triaxiality are taken into account. It should be noted that the transverse diameter of the voids is first decreasing and as the strain increases, the triaxiality imposed by the external neck of the sample increases and therefore, the transverse void dimension starts to increase.

From the results presented in Figure 8 and 9, one can conclude that coalescence defined in terms of Thomason's plastic limit load in the ligament between the voids is difficult to capture experimentally. Therefore, the only tractable and reproducible event is the point at which the ligament between the voids is broken (linkage event) and in the following sections, the term coalescence will refer to that linkage event.

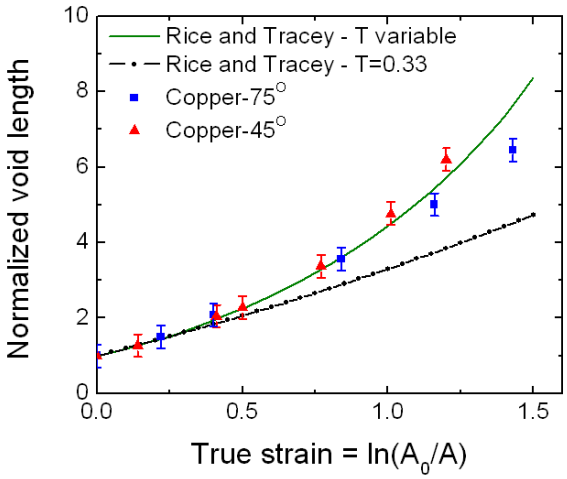

(a)

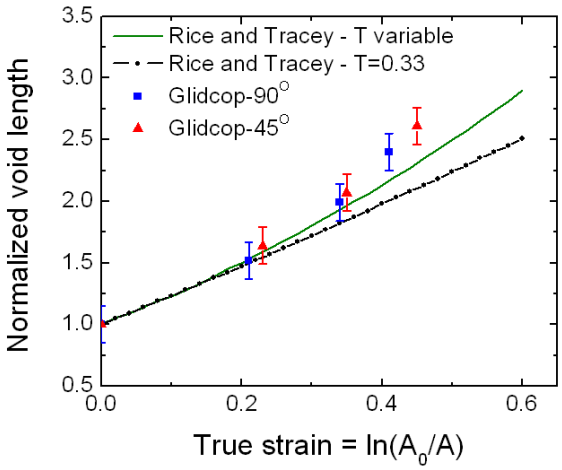

(b)

Figure 8: Comparison between the experimental results for void growth and the Rice and Tracey model with constant stress triaxiality (T=0.33) and changing stress triaxiality for (a) a copper and (b) a Glidcop sample.

4.2 Void coalescence: Brown and Embury model

The Brown and Embury model for ductile fracture states that coalescence occurs when shear bands at 45° can be drawn between the growing voids. This corresponds geometrically to the point when the void length $2a$ is equal to the intervoid spacing $2W$. This model can be easily validated by plotting both the intervoid spacing and the void major diameter as a function of the local true strain. The intersection of these two curves will then provide the coalescence

Table 1: Experimental coalescence strains (defined as $ln(A_0/A)$) for various holes configurations and materials and the corresponding predictions from the Brown and Embury model (B & E) and the Thomason model.

Material	Experiment	B & E	Difference	Thomason	Difference
Copper-75°-2W=20	0.84	0.32	-62%	0.61	-27%
Copper-45°-2W=14	1.01	0.55	-45%	0.99	-2%
Glidcop-90°-2W=75	0.41	0.23	-44%	0.58	+40%
Glidcop-45°-2W=54	0.45	0.14	-69%	0.40	-11%

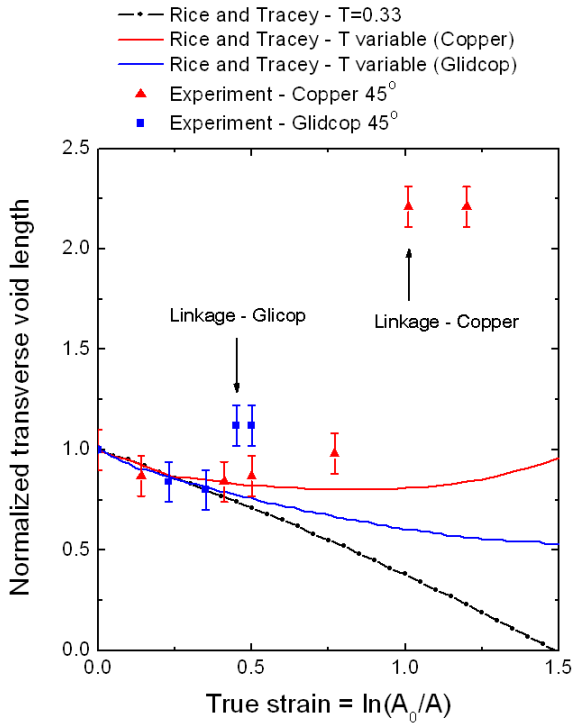

Figure 9: Comparison between the experimental results for transverse void growth and the Rice and Tracey model with constant stress triaxiality (T=0.33) and changing stress triaxiality for a copper and a Glidcop sample.

strain. The results are shown in Table 1. One can see that the differences between model and experiment are significant and of the order of 50%. This is attributed to the fact that the void is constrained by the hole-free diffusion bonded sheets which delays coalescence. Indeed, shear bands formation in the Brown and Embury model could be affected by constraining effects leading to higher stresses to deform the material and hence larger void lengths at coalescence. The constraining effects on shear banding is not taken into account in the Brown and Embury model, hence the discrepancies.

4.3 Void coalescence: Thomason model

The experimental hole configuration used here corresponds to the 3D version of the Thomason model which states that the onset of microvoid coalescence takes place when the following equation is verified:

$$\left[\frac{0.1}{(a/e)^2}+\frac{1.2}{(\frac{c}{c+e})^{1/2}}\right](1-V_f)^{-1}\left(1-(\frac{3\sqrt{\pi}}{4}V_f)^{2/3}(\frac{b}{b_0})^2e^{\varepsilon_1}\right) = \frac{\sigma_m}{Y}+\frac{3}{2}$$

where V_f is the initial void volume fraction defined as $V_f=(\pi/6)(c_0/W_0)^3$, σ_m is the mean stress, Y the plastic equivalent stress and ε_1 the applied tensile plastic strain.

As described earlier for the Rice and Tracey model, the stress triaxiality σ_m/Y varies according to equation 7. Because the Rice and Tracey equations have been validated by comparison with experiments in section 4.1 they can be used in the Thomason model.

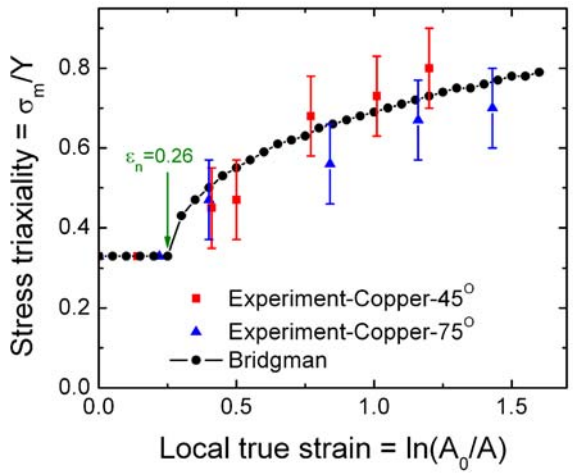

(a)

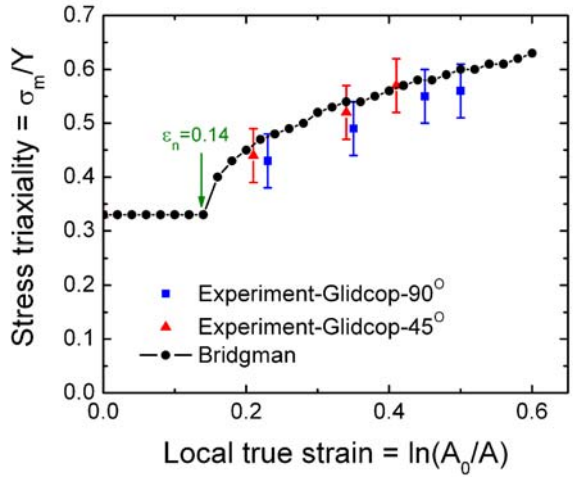

(b)

Figure 10: Stress triaxiality in the middle of (a) a copper and (b) a Gidcop sample as a function of strain. Both experimental results and the Bridgman predictions from equation 7 are presented. The stress triaxiality only increases after the necking strain ε_n defined in Figure 6.

The right hand side (RHS) and left hand side (LHS) of equation 8 are plotted against the true strain calculated from the reduction in cross sectional area of the samples and the intersection of these curves gives the coalescence strain. An example of such curves is seen in Figure 11 for copper samples. The coalescence strain results are shown in Table 1. One can see that for the copper sample failing in the direction normal to the applied strain (Copper-45°-2W=14) the failure prediction is excellent. In this case, the hole coalesce horizontally and not at 45° and so a value of 2W=28 was used in the model. Therefore, this experiment matches the assumption of the model rather well. However, for the failure path at 75° (Copper-75°-2W=20), the difference between model and experiment is significant (27%). One possible reason resides in the limit of validity of the Thomason model. Indeed, this model has been developed only for voids coalescing at 90° with respect to the tensile axis because the constraint factor represented by the first term in brackets in equation 8 has not been defined for an arbitrary angle with respect to the tensile axis. Concerning the Glidcop sample with an array of holes at 90°, one can see that the failure strain is very much overestimated by the Thomason model (40% difference). This is due to the fact that the alumina particles nucleate a secondary population of voids between the main laser drilled holes which greatly accelerates coalescence as shown in the SEM micrographs. It has already been demonstrated in the literature [31] how secondary voids greatly reduce the coalescence strain between the main growing voids. Lassance et al. [31] introduced the effect of a second void population on void coalescence into the Thomason model but using this variation of the Thomason model requires knowledge of the nucleation strain for the secondary voids and their initial volume fraction. Furthermore, a void growth law has to be defined for the growing secondary voids in the ligament between the main holes. This complicates the present analysis and has not been carried out here as the nucleation strain and void growth law for the secondary voids are not known. However it is not clear whether the observed effect is due to secondary void nucleation or whether it is due to the strong localization that occurs at low strains in Glidcop due to its much higher yield stress.

Finally, the influence of the work hardening rate on coalescence can also be studied based on the modelling work of Pardoen and Hutchinson [32]. To include the effect of the work hardening they proposed replacing the constants 0.1 and 1.2 in the Thomason model (equation 8) by respectively $\alpha(n)$ and $\beta(n)$ as follows:

$$\sigma_n/Y_{3D} = \frac{\alpha(n)}{(a/e)^2} + \frac{\beta(n)}{(\frac{c}{c+e})^{1/2}} \qquad (8)$$

where $\alpha(n)$ and $\beta(n)$ are functions of the work hardening exponent n. They found $\beta(n)$ to be almost constant, and about 1.24, while

$$\alpha(n) = 0.1 + 0.217n + 4.83n^2 \qquad (0 \leq n \leq 0.3) \quad (9)$$

When $n = 0$, the initial Thomason value is recovered. To check whether the work hardening rate has an effect on the coalescence strains for the materials studied here, the Thomason results are compared to each other using both $n = 0$ and $n = 0.3$. The results are plotted in Figure 11 for the case of the copper samples. One can see that at low strains, the LHS of equation 8 is significantly different when the work hardening is included. However, at the coalescence strains, the differences are negligible. This is consistent with the experimental results which show that at high strains, the work hardening rate of the material falls to almost zero as can be seen in Figure 6. Therefore, one can conclude that the work hardening rate has little effect when the material can deform up to high strains. This might however not be the case under high stress triaxiality which would significantly raise the RHS curve in Figure 11 or for materials that exhibit void coalescence at low strains.

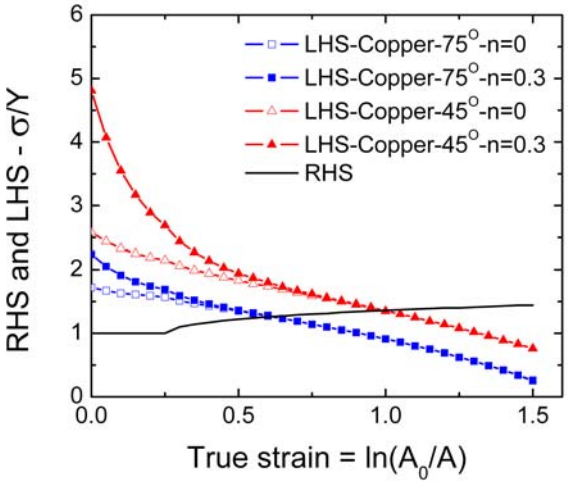

Figure 11: Comparison between the coalescence strain predictions using the Thomason model (equation 8) with two different hardening exponents: $n = 0$ and $n = 0.3$.

5 Conclusion

Using laser-drilled materials and x-ray computed tomography, void growth and coalescence were captured in detail inside copper based samples. The strong effect of macroscopic necking on the coalescence path is demonstrated. It is also shown that material strength and nucleation of secondary voids result in greatly reduced coalescence strains.

The Rice and Tracey model gives good predictions of void growth rates, because voids are quasi-spherical and stress triaxiality variations with strain are taken into account.

The void lengths at coalescence predicted by the Brown and Embury model are smaller than experimental values. This is due to constraining effects which delay coalescence.

The Thomason model gives excellent predictions for copper samples containing holes coalescing normal to the tensile axis. For the other configuration (holes at 75°), the prediction is poor since the model does not account for holes oriented at an arbitrary angle with respect to the tensile axis. The Thomason model also overestimates the failure strains in the case of Glidcop samples because of secondary void nucleation which precipitates failure.

Because coalescence strains were fairly high and stress triaxialities were relatively low, the work hardening rate of materials at coalescence was almost zero; therefore, there was no need to take it into account.

Finally we showed that it is possible to obtain quantitative and reproducible information on the

ductile fracture process. It has been shown that coalescence models in literature have been proposed for specific configurations (holes normal to the tensile axis) and need to be developed to account for what is seen experimentally such as coalescence by shear.

Acknowledgement

We gratefully acknowledge the support of the Natural Sciences and Engineering Research Council of Canada (NSERC). Also, we thank M. Di Michiel, J. Adrien and H. Muto for assistance with the tomography experiments at ESRF and K. Uesugi for the tomography experiments at SPring-8.

References

[1] Goods S., Brown L. Acta Metallurgica 1979; 27: 1-15.

[2] Babout L., Ludwig W., Maire E., Buffière J. Nuclear Instruments and Methods in Physics Research Section B 2003; 200: 303-307.

[3] Argon A.S., Im J., Safoglu R. Metallurgical Transactions A 1975; 6A: 825-837.

[4] Puttick K.E. Philosophical Magazine 1959; 4: 964-969.

[5] Floreen S., Hayden H. Scripta Metallurgica 1970; 4: 87-94.

[6] Cox T.B., Low J.R.J. Metallurgical Transactions 1974; 5: 1457-1470.

[7] McClintock F. J. Appl. Mech. 1968; 35: 363-371.

[8] Rice J., Tracey D. Journal of the Mechanics and Physics of Solids 1969; 17: 201-217.

[9] Gurson A. Journal of Engineering Materials and Technology 1977; 99: 2-15.

[10] Thompson A. Metallurgical Transactions A 1987; 18A: 1877-1886.

[11] Knott J. Metal Science 1980; 327–336.

[12] Park I.-G., Thompson A.W. Acta Metallurgica 1988; 36: 1653-1664.

[13] Marini B., Mudry F., Pineau A. Engineering Fracture Mechanics 1985; 22: 989-996.

[14] Brown M., Embury D. In: Proceedings of 3rd International Conference on Strength of Metals and Alloys 1973; Institute of Metals, London: 164-169.

[15] Needleman A., Tvergaard V. Journal of the Mechanics and Physics of Solids 1984; 32: 461-490.

[16] Thomason P. Journal of the Institute of Metals 1968; 96: 360-365.

[17] Babout L., Maire E., Buffière J., Fougères R. Acta Materialia 2001; 49: 2055-2063.

[18] Gammage J., Wilkinson D., Brechet Y., Embury D. Acta Materialia 2004; 52: 52555263.

[19] Magnusen P.E., Dubensky E.M., Koss D.A. Acta Metallurgica 1988; 36: 1503-1509.

[20] Jia S., Povirk G. International Journal of Solids and Structures 2002; 39: 25332545.

[21] Nagaki S., Nakayama Y., Abe T. International Journal of Mechanical Sciences 1998; 40: 215-226.

[22] Weck A., Crawford T.H.R., Borowiec A., Wilkinson D.S., Preston J.S. Applied Physics A-Materials Science and Processing 2007; 86: 55-61.

[23] Uesugi K., Suzuki Y., Yagi N., Tsuchiyama A., Nakano T. Nuclear Instruments and Methods in Physics Research Section A: Accelerators, Spectrometers, Detectors and Associated Equipment 2001; 467-468: 853-856.

[24] Di Michiel M., Merino J.M., Fernandez-Carreiras D., Buslaps T., Honkimaki V., Falus P., Martins T., Svensson O. Review of Scientific Instruments 2005; 76: 4.

[25] Buffière J.-Y., Maire E., Cloetens P., Lormand G., Fougères R. Acta Materialia, 1999; 47: 1613-1625.

[26] Thomason P.F. Ductile Fracture of Metals. Oxford: Pergamon Press; 1990.

[27] Rousselier, G., Nuclear Engineering and Design, 1987; 105: 97-111.

[28] Zhang, Z. L. and Niemi, E. International Journal of Fracture, 1994; 70: 321-334.

[29] Bridgman P.W. Studies in Large Plastic Flow and Fracture New York: 1952.

[30] Zhang Z. L., Hauge M., Odegard J., Thaulow C. International Journal of Solids and Structures, 1999; 36: 3497-3516.

[31] Lassance D., Fabregue D., Delannay F., Pardoen T. Progress in Materials Science 2007; 52: 62-129.

[32] Pardoen T., Hutchinson J.W. Journal of the Mechanics and Physics of Solids 2000; 48: 24672512.